Nature Letter

Colour cycling on 67P/CG coma and nucleus

Gianrico Filacchione[1*], Fabrizio Capaccioni[1], Mauro Ciarniello[1], Andrea Raponi[1], Giovanna Rinaldi[1], Maria Cristina De Sanctis[1], Dominique Bockelèe-Morvan[2], Stèphane Erard[2], Gabriele Arnold[3], Vito Mennella[4], Michelangelo Formisano[1], Andrea Longobardo[1], Stefano Mottola[3] and VIRTIS team

[1] INAF-IAPS, Institute for Space Astrophysics and Planetology, via del Fosso del Cavaliere, 100, 00133 Rome - Italy
[2] LESIA, Observatoire de Paris, Universitè PSL, CNRS, Sorbonne Universitè, Univ. Paris Diderot Sorbonne Paris Citè F-92195 Meudon, France
[3] German Aerospace Center (DLR), Institute of Planetary Research, Berlin, Germany
[4] INAF-Osservatorio Astronomico di Capodimonte, Naples, Italy

*) Corresponding author: gianrico.filacchione@inaf.it

SUMMARY

The solar heating reaching a cometary surface provides the energy input necessary to sustain gaseous activity through which dust is removed from the nucleus [1,2]. In this dynamical environment, both coma [3,4] and nucleus [5,6] evolve during the orbit, changing their physical and compositional properties. The environment encircling an active cometary nucleus is populated by dust grains with complex and variegated shapes [7] lifted and diffused by gases freed from the sublimation of surface ices [8,9]. Visible colour of dust particles is highly variable: carbonaceous-organic material-rich grains [10] appear red while Mg-silicate [11] or water ice [12] rich grains are blue with further dependence from grain size distribution, viewing geometry, activity level and comet family type.
Here we report about the observation of two opposite seasonal colour cycles developing in the coma dust particles and on the surface of comet 67P/CG as observed by Rosetta spacecraft during its perihelion passage in 2015 [13]. Spectral analysis indicates an enrichment of submicron grains made of organic material and amorphous carbon in the coma causing the escalating colour reddening observed during the perihelion passage. At the same time, the progressive removal of dust from the nucleus causes the exposure of more pristine and bluish icy layers on the surface. Far from the Sun, we find that the abundance of water ice on the nucleus is reduced due to redeposition of dust and/or dehydration of the surface layer while water ice or possibly Mg-silicate grains contribute to bluish coma's colours.

MAIN TEXT

Understanding how comets work and evolve is one of the most compelling questions to which the Rosetta mission has been trying to answer. Differently from previous space missions (International Cometary Explorer at 21P/Giacobini-Zinner in 1985; Vega 1-2, Sakigake, Suisei and Giotto at 1P/Halley in 1986; Giotto at 26P/Grigg-Skjellerup in 1992; Deep Space 1 at 19P/Borrelly in 2001; Stardust at 81P/Wild 2 in 2004; Deep Impact at 9P/Tempel 1 in 2005, then renamed EPOXI at 103P/Hartley 2 in 2010)

which were flying fast flybys in the surroundings of cometary nuclei at a given point of their orbits, Rosetta was capable to escort comet 67P/Churyumov-Gerasimenko during the entire perihelion passage allowing to continuously monitor the temporal evolution of its visible colours as a function of the heliocentric distance. By integrating spacecraft with telescopic data from the Earth, we know that many comets observed so far are characterized by red-coloured coma dust particles [10], a spectral behaviour typical of refractory materials. Local colour changes are associated with grain size variations, like in the bluer jets made of submicron grains on comet Hale-Bopp [14] or in fragmented grains on C/1999 S4 (LINEAR) coma [15]. Apart from grain size, also composition influences coma's colour response because transparent volatiles, like water ice and organics [16,12] or Mg-rich silicates [11,17] can introduce a significant blueing in scattered light (see discussion in the Methods). A similar effect has been observed in the dust particles ejected after Deep Impact event [18]. The long duration of the Rosetta mission [13] gives us the unique opportunity to follow the colour changes developing on 67P comet nucleus and coma in its active phase through the inner Solar System. So far, several studies have investigated how dust and gas (H_2O, CO_2) production are correlated among them during one cometary rotation showing that the water ice sublimation on 67P surface is the driving mechanism for dust ejection in the coma [2]. However, the dust emission flux appears lower above high-cohesion consolidated terrains while it is maximum when the subsolar direction is aligned above volatile-rich areas. Since the illumination conditions continuously change, rather than focusing on coma and nucleus colours variations occurring during few diurnal rotations, we analyse the entire dataset returned by VIRTIS, the Visible, Infrared and Thermal Imaging Spectrometer [19] which includes a multitude of data collected from January 2015 (inbound orbit, heliocentric distance 2.55 AU), encompassing perihelion passage (August 2015, 1.24 AU) until May 2016 (outbound orbit, 2.92 AU). Spectral indicators in the visible range, including the integrated radiance (I), the wavelength of the radiance peak (λ_{max}) and the spectral slopes (in the 0.4-0.5 and 0.5-0.8 μm ranges), are synergistically used to model composition and grain size distribution of the dust particles in the coma as a function of heliocentric distance. Those spectral indicators are derived for each spectrum acquired by VIRTIS in an annulus encircling the nucleus and comprising all the pixels in the coma located at a tangent altitude between 1 and 2.5 km above the nucleus' limb. At the same time, we monitor the colour changes occurring on 12 test-areas on the nucleus through the 0.5-0.8 μm spectral slope [5,6]. The description of the dataset, including an example of VIRTIS images and spectra after calibration improvement, spectral indicators processing, and data modeling, are given in the Methods.

From a synergistic analysis of the spectral properties of the coma and of the nucleus surface, two opposite trends with heliocentric distance are observed. Coma integrated radiance increases (see I time-series in Figure 1 a) and colour becomes redder when the comet approaches perihelion (see λ_{max}, 0.4-0.5 and 0.5-0.8 μm spectral slopes time-series in Figure 1 b-c-d). Conversely, on twelve control areas of the nucleus, for which we have continuous time-coverage during the entire Rosetta mission, we observe a systematic blueing of the surface (see 0.5-0.8 μm spectral slopes time-series in Figure 2), with a reduction of the spectral slope up to 50% measured between 67P's passage through the frost line (heliocentric distance 2.7 AU, occurring in October 2014 during inbound orbit and in April 2016 on the outbound) and perihelion (1.25 AU, August 2015). During the pre-perihelion period, we interpret the coma colour change as being the consequence of the progressive loss of the ice fraction in the dust grains ejected from the nucleus [20], which makes them redder.

When the comet approaches the Sun, the dust grains lifted from the nucleus' south hemisphere, the one illuminated at that time, are warmer and become more dehydrated. Simulations based on Mie scattering theory applied to spherical grains of radius between 0.1 and 50 μm and five different compositions (see Methods) are used to model VIRTIS spectral indicators, e.g. λ_{max} and 0.5-0.8 μm spectral slope. Simulation results (Figures 3-4) are compatible with the presence of submicron grains made of organic matter and carbon during perihelion passage which could be the result of the fragmentation of mineral and organic matrix embedded in larger grains. During the outbound orbit, the simulations show that the organic material continues to be present in the coma together with an increasing percentage of different grains (water ice or Mg-silicate; both are not fully compatible with spectral indicators trends, see ED-Table 3) contributing to the progressive blueing observed in the data. In this orbital phase, the Sun shines again on the northern hemisphere, from where a greater flux of surficial water ice-rich grains [21] is lifted in the coma.

Conversely, the nucleus' surface becomes progressively bluer during the inbound orbit because the greater solar input causes an increase of the gaseous activity. This triggers dust ejection with consequent erosion of the surface: on average, a 0.5 m thick erosion layer is lost during each orbit [21]. As a result of this process, more pristine subsurface layers enriched in water ice are exposed on the surface, which turns bluer [5,6,22]. We have evidence [6], in fact, that water ice-rich layers are immediately available under the dust layer, as shown in areas of recent disruption of the surface [23] and as demonstrated by many thermal models applied to cometary nuclei [24,25]. Between 20% [21] to 50% [26] of the dust grains ejected around perihelion from the south pole, the region which receives the maximum insolation at that time, fall-back preferentially on the northern hemisphere. The fall-back flux is dominated by decimetre-sizes dust aggregates in which a small fraction of water ice can be maintained [21]. After perihelion, as soon as activity begins to settle, the progressive accumulation of dust on the surface covers again the exposed pristine layers making the nucleus surface redder again. This process explains the colour cycle observed by VIRTIS on the nucleus (Figure 2).

Colour of 67P coma particles can be modelled with submicron to 50 μm radius grains made of water ice before perihelion, organic material and carbon at perihelion, and water ice or possibly Mg-silicate grains after perihelion. Similar composition endmembers are compatible with the findings reported by previous Rosetta's studies. On infrared spectra of 67P coma by VIRTIS-M, a broad absorption feature in the 3.0-3.7 μm spectral range, consistent with a composition made of water ice mixed with organic materials, has been observed [27]. During outbursts, a broad emission feature between 3.4 and 3.6 μm has been detected [28] resulting compatible with the sublimation of organic materials caused by the high temperatures of the grains. Finally, the colour reduction observed when the comet was far from the Sun resembles water ice grains spectral properties, as indicated by other studies: thermal models and OSIRIS camera images [20] show that at 1.53 AU heliocentric distance the total sublimation of ice for grains of radius between 5 and 500 μm made of ice-dust layers or mixtures occurs well-beyond the 2.5 km distance from 67P nucleus considered here. This implies that water ice grains can still populate the region of the coma analysed in this work. Moreover, a photometric investigation of the visible colours of more than a thousand individual grains imaged by OSIRIS camera in 67P coma [29] indicates the presence of three composition classes including organic material grains (steep colour slope), mixtures of silicate and organic material (intermediate slope) and water ice (flat slope). The presence of carbon, silicates and magnesium on 67P dust grains has been assessed by the COSIMA instrument on Rosetta [30]. Apart water ice,

Mg-silicates particles are among the best spectral candidates to reproduce the blue coloured coma observed from Earth on many different comets [11,17] and we cannot exclude their presence also in 67P coma during the post perihelion period.

VIRTIS results confirm these previous findings on dust particles composition by modeling their scattering behaviour on a wide range of viewing geometries. The extended temporal coverage encompassing different orbital phases shows an anticorrelation between the colour variations of the dust in the coma and the nucleus surface on 67P.

Statement of individual contributions: the paper is a collective effort by VIRTIS dust working group. FG as main author of the paper has calibrated, processed and interpreted VIRTIS data. FC as VIRTIS PI has managed the experiment; MC, AR, GR have supported with Mie scattering calculations and data processing; FC and DBM have planned 67P coma observations by VIRTIS; FC and GF have planned 67P nucleus observations by VIRTIS; SE has provided geometry files for coma and nucleus observations; all authors have contributed to the discussion of the results.

REFERENCES IN MAIN TEXT

[1] Gundlach, B., et al., What drives the dust activity of comet 67P/Churyumov-Gerasimenko? Astron. Astrophys., 583, A12 (2015).

[2] Tubiana, C. et al., Diurnal variation of dust and gas production in comet 67P/Churyumov-Gerasimenko at the inbound equinox as seen by OSIRIS and VIRTIS-M on board Rosetta, Astron. Astrophys., in press, arXiv:1905.03022

[3] Hansen, K. C. et al., Evolution of water production of 67P/Churyumov-Gerasimenko: An empirical model and a multi-instrument study, Mon. Not. R. Astron. Soc., 462, S491-S506 (2016).

[4] Bockelée-Morvan, D. et al., VIRTIS-H observations of comet 67P's dust coma: spectral properties and color temperature variability with phase and elevation, Astron. Astrophys., in press, arXiv: 1901.03074 (2019).

[5] Filacchione, G. et al., The global surface composition of 67P/CG nucleus by Rosetta/VIRTIS. (I) Prelanding mission phase, Icarus, 274, 334-349 (2016).

[6] Ciarniello, M. et al., The global surface composition of 67P/Churyumov-Gerasimenko nucleus by Rosetta/VIRTIS. II) Diurnal and seasonal variability, Mon. Not. R. Astron. Soc., 462, S443-S458 (2016).

[7] Güttler, C. et al., Synthesis of the Morphological Description of Cometary Dust at Comet 67P, Astron. Astrophys., in press, arXiv:1902.10634 (2019).

[8] Huebner, W.F., Benkhoff, J., Capria, M. T., Coradini, A., De Sanctis, C., Orosei, R., Prialnik, D. (eds.), Heat and Gas Diffusion in Comet Nuclei, SR-004, June, 2006. ISBN 1608-280X. Published for The International Space Science Institute, Bern, Switzerland, by ESA Publications Division, Noordwijk, The Netherlands (2006).

[9] Läuter, M. et al., Surface localization of gas sources on comet 67P/Churyumov-Gerasimenko based on DFMS/COPS data, Mon. Not. R. Astron. Soc., 483, 852-861, (2019).

[10] Jewitt, D. and Meech, K.J., Cometary grain scattering versus wavelength, or, "What color is comet dust?", Astrophys. J. Lett. 310, 937-952 (1986).

[11] Zubko, E., et al., Interpretation of photopolarimetric observations of comet 17P/Holmes. J. Quant. Spectrosc. Radiat. Transf., 112, 1848-1863 (2011).

[12] Beer, E., The grain evolution model for icy grains ejected from 9P/Tempel 1 by Deep Impact, in Deep Impact as a World Observatory Event: Synergies in Space, Time and Wavelengths, ed. by H.U. Kaüfl, C. Sterken (Springer, Berlin), 59-67, (2009).

[13] Taylor, M.G.G.T. et al., The Rosetta mission orbiter science overview: the comet phase. Phil. Trans. R. Soc. of London S., A 375, 20160262 (2017).

[14] Furusho, R. et al., Imaging polarimetry and color of the inner coma of comet Hale-Bopp (C/1995 O1), Publ. Astron. Soc. Jpn. 51, 367-473 (1999).

[15] Hadamcik, E. and Levasseur-Regourd, A.C., Dust coma of comet C/1999 S4 (LINEAR): imaging polarimetry during nucleus disruption, Icarus, 166, 188-194 (2003).

[16] Fernàndez, Y.R. et al., Near-infrared light curve of comet 9P/Tempel 1 during Deep Impact, Icarus, 187, 220-227 (2007).

[17] Hadamcik, E., et al., Linear polarization of light scattered by cometary analogs: new samples, in Asteroids, Comets and Meteors 2014, Helsinki, Finland (2014).

[18] Hodapp, K.W. et al., Visible and near-infrared spectrophotometry of the Deep Impact ejecta of comet 9P/Tempel 1, Icarus, 187, 185-198 (2007).

[19] Coradini, A. et al., Virtis: An Imaging Spectrometer for the Rosetta Mission, Sp. Sci. Rev., 128, 529-559 (2007).

[20] Gicquel, A., et al., Sublimation of icy aggregates in the coma of comet 67P/Churyumov-Gerasimenko detected with the OSIRIS cameras on board Rosetta, Mon. Not. R. Astron. Soc., 462, S57-S66 (2016).

[21] Keller, H. U. et al., Seasonal mass transfer on the nucleus of comet 67P/Chuyumov-Gerasimenko, Mon. Not. R. Astron. Soc., 469, S357-S371 (2017).

[22] Fornasier, S., Rosetta's comet 67P/Churyumov-Gerasimenko sheds its dusty mantle to reveal its icy nature, Science, 354, 1566-1570 (2016).

[23] Filacchione, G. et al., Exposed water ice on the nucleus of comet 67P/Churyumov-Gerasimenko, Nature, 529, 368-372 (2016).

[24] De Sanctis, et al. Thermal evolution model of 67P/Churyumov-Gerasimenko, the new Rosetta target, Astron. Astrophys., 444, 605 (2005).

[25] Capria, M. T. et al., How pristine is the interior of the comet 67P/Churyumov-Gerasimenko? Mon. Not. R. Astron. Soc., 469, S685-S694 (2017).

[26] Hu, X. et al., Seasonal erosion and restoration of the dust cover on comet 67P/Churyumov-Gerasimenko as observed by OSIRIS onboard Rosetta, Astron. Astrophys., 604, A114 (2017).

[27] Rinaldi, G., et al., Cometary coma dust size distribution from in situ IR spectra, Mon. Not. R. Astron. Soc., 469, S598-S605 (2017).

[28] Bockelée-Morvan, D. et al., Comet 67P outbursts and quiescent coma at 1.3 AU from the Sun: dust properties from Rosetta/VIRTIS-H observations, Mon. Not. R. Astron. Soc., 469, S443-S458 (2017).

[29] Frattin, E. et al., Post-perihelion photometry of dust grains in the coma of 67P Churyumov-Gerasimenko, Mon. Not. R. Astron. Soc., 469, S195-S203 (2017).

[30] Bardin, A. et al., Carbon-rich dust in comet 67P/Churyumov-Gerasimenko measured by COSIMA/Rosetta, Mon. Not. R. Astron. Soc., 469, S712-S722 (2017).
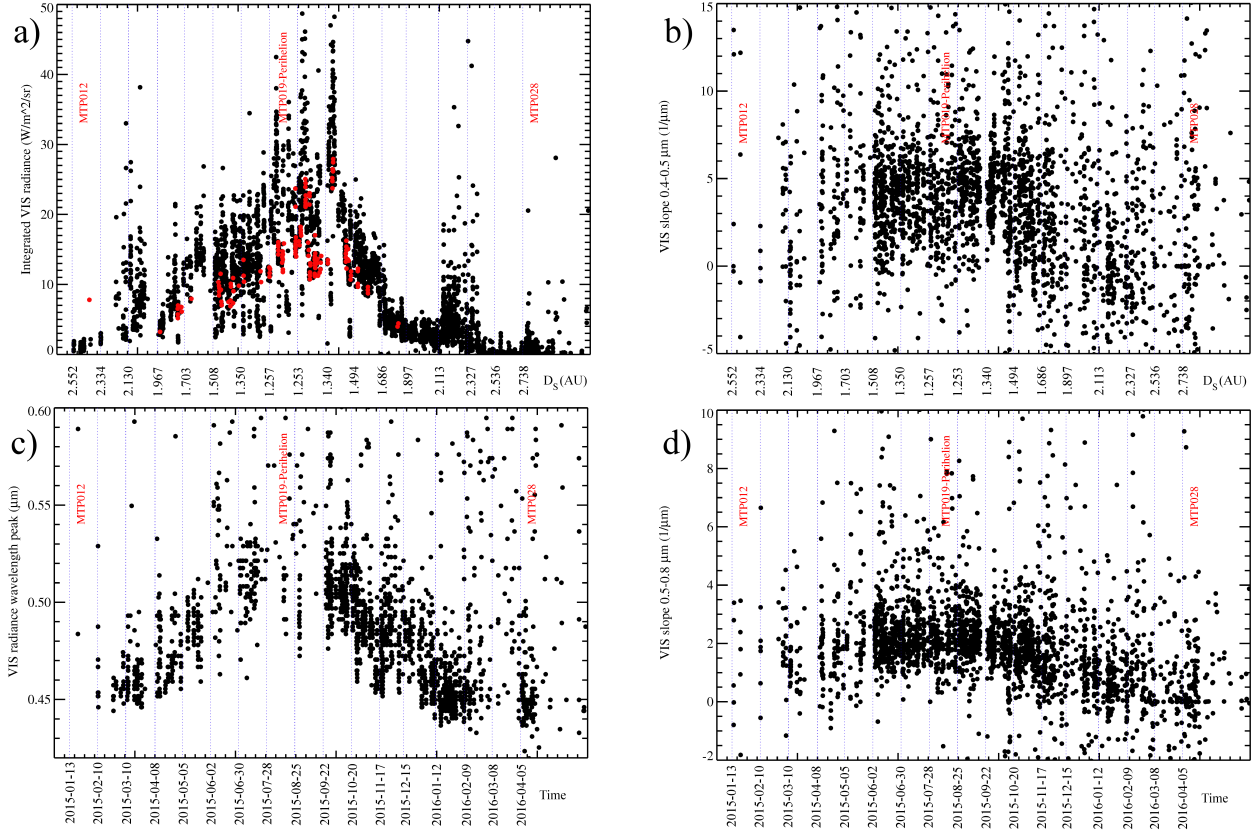
Figure 1. Time-series of the spectral properties of 67P coma dust. Panel a) Integrated radiance (I): full dataset, partial annulus coverage (black points); reduced dataset, complete annulus coverage (red points, see discussion in Methods section); b) 0.4-0.5 μm spectral slope; c) visible radiance wavelength peak λ_{max} ; d) 0.5-0.8 μm spectral slope. Through the paper spectral slopes are given in 1/μm corresponding to 10%/100 nm colour slope. Rosetta's MTP intervals are marked by vertical lines between MTP012 and MTP028. Time intervals of MTP periods are listed in Table 1 in the Methods. Perihelion occurs during MTP019.

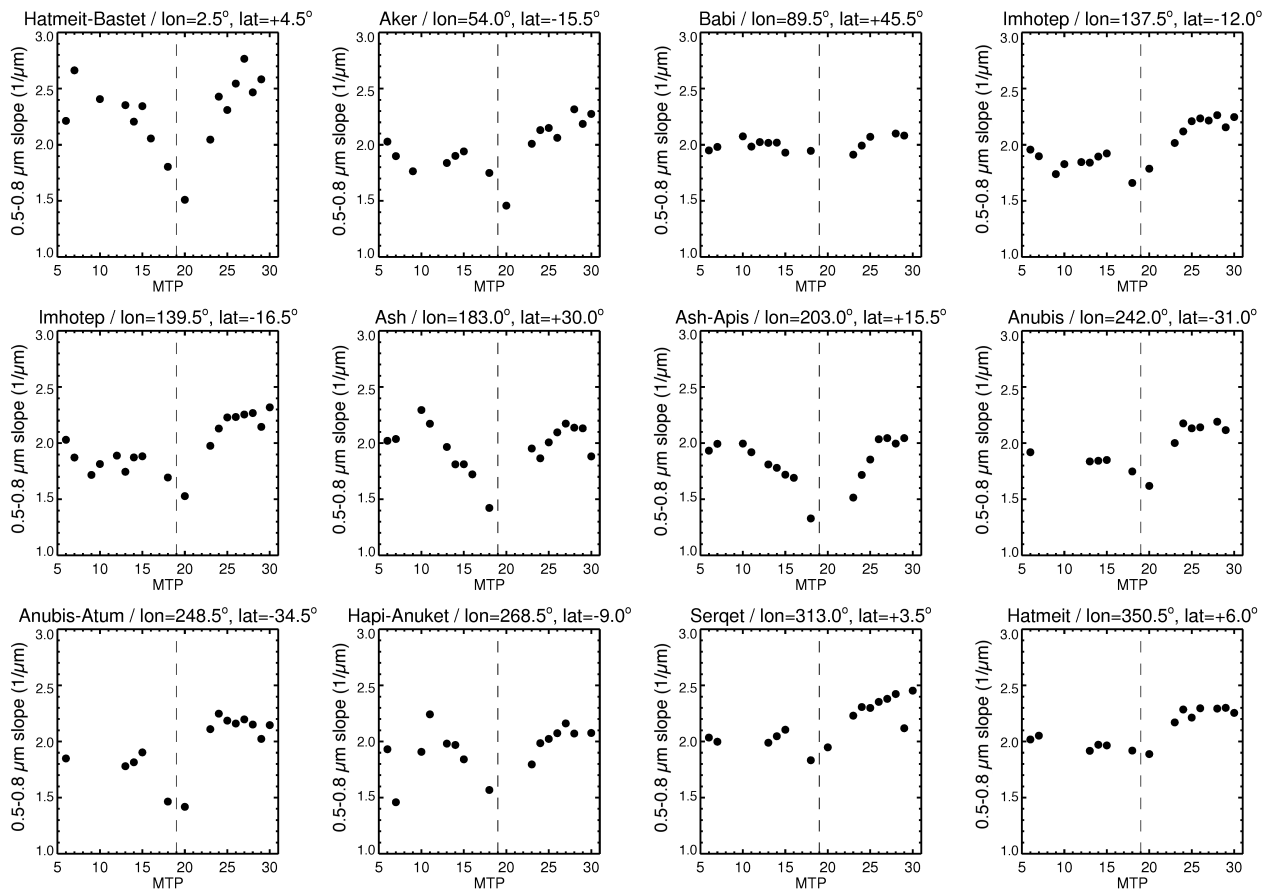Figure 2. Time evolution of 67P nucleus colour measured through the 0.5-0.8 μm spectral slope above 12 control areas of 67P surface. Perihelion passage occurs during MTP019 and is marked by the vertical dash line. The morphological region name and position (longitude, latitude) of each area are reported in the plots captions. The maximum error associated to the slope measurements is of the order of ±0.1 μm^{-1}.
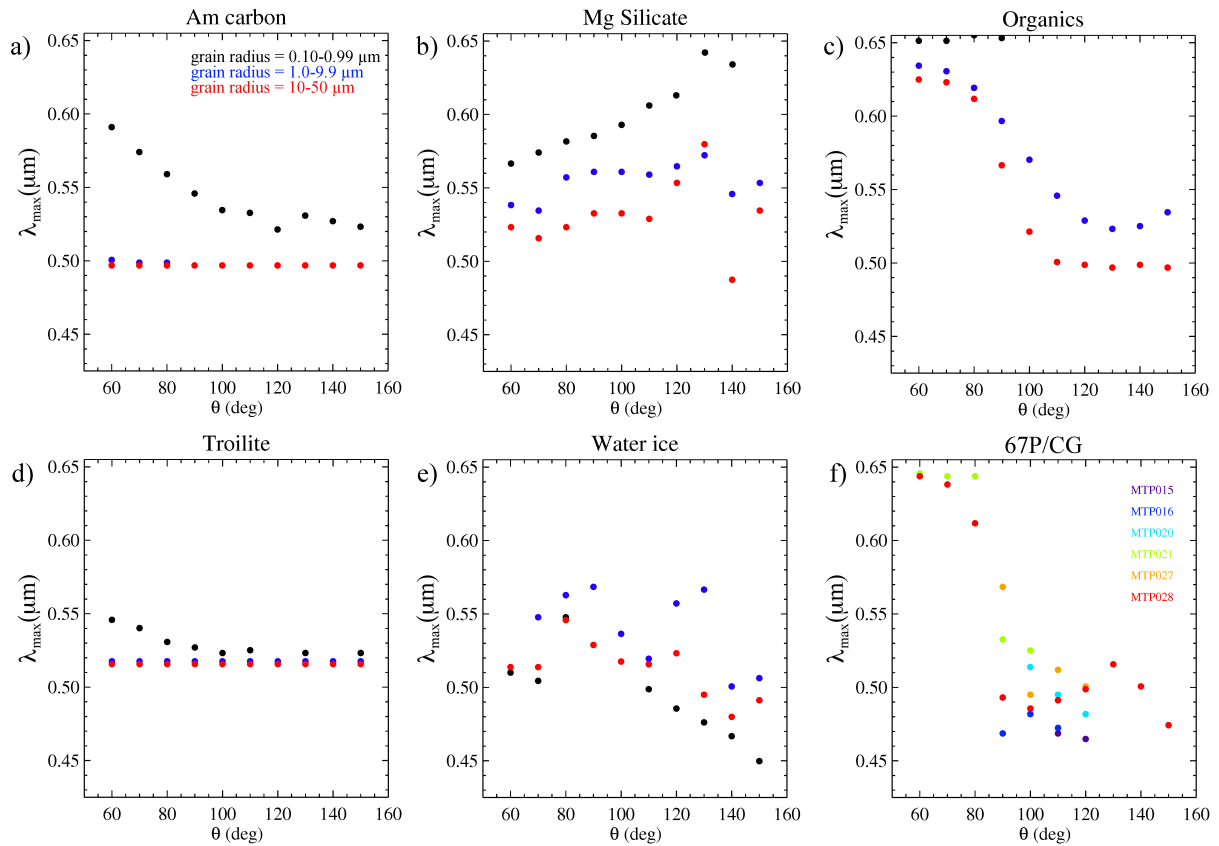
Figure 3. Theoretical model results of the λ_{max} trends as function of composition and grain radius distribution. Panel a: amorphous carbon. Panel b: Mg-silicate. Panel c: organic ice tholin (λ_{max} >0.65 for 0.10-0.99 μm radius grains). Panel d: troilite. Panel e: water ice. Panel f: 67P/CG observations by VIRTIS, median data computed on 10° bins scattering angles during different mission phases. Standard deviation computed on VIRTIS data is of the order of 0.03 μm.
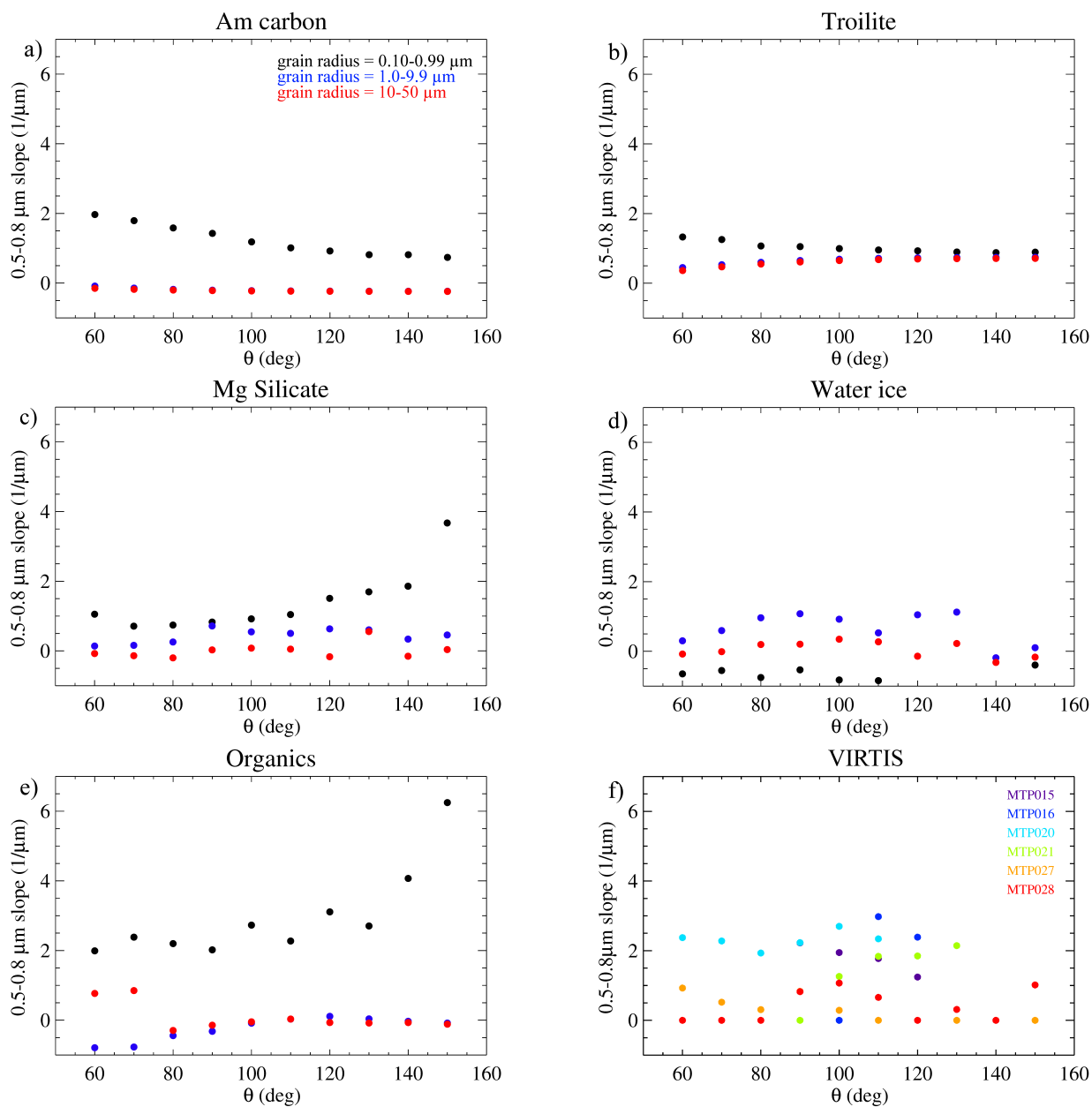
Figure 4. Simulations of the 0.5-0.8 μm spectral slope as a function of the scattering angle θ for spherical particles of different composition: amorphous carbon (panel a), troilite (b), Mg-silicate (c), water ice (d), organics (e). Median spectral slope derived from VIRTIS observations for pre-perihelion (MTP015-016), perihelion (MTP020-021) and post-perihelion (MTP027-028) mission phases are shown in panel f). The standard deviation of VIRTIS data is ≤0.6 μm^{-1}.

METHODS

VIRTIS dataset

While the scientific objectives of the Rosetta mission [13], including the study of the dust in the coma, were well-defined before the spacecraft reached 67P, the detailed planning of the scientific payload operations has been a complex and continuously evolving process due to the uncertainties of the cometary environment in which the mission had to operate. A detailed overview of the Rosetta science planning process and challenges is given in [31]. In this context, VIRTIS coma observations were performed from very different viewing and illumination geometries, spacecraft ranges from the nucleus, heliocentric distances and cometary activity levels resulting in a dataset showing a very variable spatial resolution and signal to noise ratio.

While VIRTIS-led targeted observations of the coma have been routinely executed, a large fraction of the VIRTIS dataset consisted of ridealong and serendipitous acquisitions which have been acquired while the spacecraft attitude and pointing were controlled by other instruments. For this reason, to maximize the retrieval of information about the dust particles properties, a statistical approach has been applied to the vast VIRTIS-M-VIS dataset with the scope to exploit it in its completeness.

We restrict our analysis only to the VIRTIS-M (imaging channel) VIS data covering the 0.25-1.0 μm spectral range with 432 bands and a spectral sampling <2 nm/band. A detailed description of the VIRTIS experiment is provided by [19]. Differently from the VIRTIS-M IR channel operating within the 1-5 μm spectral range, which ceased the operations on May 2015 due to a permanent failure of the cryocooler dedicated to the cooling of the IR channel detector, the VIS channel has operated flawlessly for the entire duration of the mission.

For this work we have processed coma data collected during Rosetta's MTP012-028 periods. The time intervals of each MTP (Medium Term Phase) are listed in Extended Data Table 1. The dataset consists of more than 4,500 hyper spectral cubes of the coma of 67P acquired from a range of distances from the nucleus between 27.8 to 1462.2 km, resulting in a spatial resolution between 7 and 365 m/pixel, respectively.

Each VIRTIS observation has been calibrated in spectral radiance [32] and specific geometry parameters have been computed for each pixel falling on the coma region and the nucleus. Further details about the VIRTIS data mapping methods are given by [5]. The nucleus solar phase and the spacecraft position and distance in the cartesian frame centred on the nucleus have been computed using SPICE kernels [33].

The spectral parameters used in our analysis to study the coma emission are computed in an annulus defined by a tangent altitude running between a_{min}=1 km and a_{max}=2.5 km around the nucleus. This criterion is adopted independently from the nucleus-spacecraft distance and the solar phase angle at the time of the observation. The selection of pixels placed at distances larger than 1 km allows 1) to reduce the contribution of the instrumental stray-light coming from the illuminated part of the nucleus and 2) to maximize the coverage across the dataset.

An example of a VIRTIS-M-VIS image of the coma showing the annulus definition is given in Extended Data Figure 1 - top panels. This particular image refers to observation

MTP019 - STP068 - V1_00397724286 acquired on August 9th 2015 from a distance of 304 km, resulting in a spatial resolution of 75 m/px with an integration time of 16 sec/line.

Such a viewing geometry is not very common because the completeness of the annulus over the 360 degrees azimuth (up to distance a_{max}) is limited by the instrumental Field Of View (FOV=3.6°), by the relative distance (d) between Rosetta spacecraft and comet's surface and by the spacecraft offnadir pointing direction (α). Only when the following condition is verified VIRTIS-M can acquire the full annulus:

$$\alpha + arctg\left(\frac{a_{max}+r}{d}\right) \leq FOV \qquad 1.)$$

where r=1.74 km is the average radius of the nucleus [34]. A similar condition is verified only in 248 observations (marked as red points in Figure 1-a), corresponding to about 5% of the dataset: as a consequence, integrated radiance and maximum emission wavelength values could be biased by the incompleteness of the annulus on the remaining observations. The average integrated radiance on incomplete annulus observations (black points) appears in general higher than on the ones where the annulus is entirely acquired (red points). This happens because VIRTIS is preferentially observing the coma towards the solar direction to maximise the signal to noise ratio. Apart from the above limitations, which introduce some scattering in the data points, the value of the integrated radiance is mainly driven by the number of scatterers (dust grains) along the line of sight, rather than on their composition and grain size distribution: spectral slopes and the spectral position of the radiance peak depend from them.

The overall coma brightness and spectral properties measured by VIRTIS are driven by light scattering on dust particles and are not altered by emissions from gas molecules in the coma. The instrument sensitivity at visible wavelengths in fact is not enough to measure gaseous emissions from CN, C_2, C_3.

Calibration update using stellar observations

With the scope to improve VIRTIS-M-VIS response in the 0.25-0.45 μm spectral range, where the standard pipeline suffers large uncertainties due to straylight introduced by the on-ground calibration setup, we have applied a radiometric correction based on stellar observations. The average signal derived from Vega (α Lyrae) observations listed in Extended Data Table 2 is used as a reference to correct the standard responsivity. Four observations of Vega acquired with the longest possible integration time, 50 s, are used to retrieve the raw signal above the noise level (about ±2 DN) estimated on the nearby deep sky pixels.

Before this step, each observation is dark-level-subtracted and despiked (see Extended Data Figure 2-top left panel, showing the signal and sky level for one of the four Vega observations). Due to the instrumental point spread function and spectral tilt, both described in detail in [35], the Vega spectral signal is distributed across 18 spatial pixels and is averaged above these. The four observations are processed in the same way before being further averaged to improve the SNR. The resulting Vega average signal is shown in Extended Data Figure 2-top right panel. The fractional deviation of the single spectra from the average is about 0.05. The Vega flux by [36] is convolved with the VIRTIS gaussian response (FWHM=2.3 nm) and then by a 4 nm wide boxcar. The spectra are then placed on an absolute wavelength scale using the centre of Balmer and Paschen intense absorption lines as references and assuming a constant dispersion. The spectral

dispersion (in nm) applied is λ(b)=232.9 + 1.88515×b, with b from 0 to 431 corresponding to VIRTIS-M number of spectral bands. The resulting relative responsivity derived as the ratio between VIRTIS signal and Vega flux is shown in Extended Data Figure 2-bottom left panel. To further remove residual high-frequency noise due to the low Vega signal, a 9-band running boxcar filter is applied. The response curves are normalized at the value of 58.75 at λ=0.635 μm to allow a direct comparison with the standard pipeline responsivity shown in Extended Data Figure 2-bottom right panel. Within the limits of the low Vega signal in the blue spectral range (less than 40 DN at 0.55 μm), this method allows to retrieve a better responsivity at shorter wavelengths with respect to the standard pipeline [35]. As shown by the ratio plot (blue curve) the standard pipeline overestimates the target radiance for wavelengths λ< 0.4 μm. On the remaining spectral range, the differences are much smaller. Since the wavelength of the dust emission spectral radiance peak occurs between 0.45 and 0.55 μm, such an instrument response correction allow to improve the retrieval of left-wing of the radiance peak and the spectral slope determinations.

Coma spectral indicators

After averaging the coma signal within the annulus previously defined and applied the updated responsivity function, we compute four spectral indicators on each observation. The indicators are 1) the integrated radiance (I) across the VIS spectral range, defined as:

$$I = \frac{\sum_{n=1}^{N} \int_{0.25\,\mu m}^{1\,\mu m} R(n,\lambda)d\lambda}{N} \quad (1)$$

where R(n,λ) is the spectral radiance measured on the n-th pixel of the annulus at wavelength λ and N is the total number of pixels within the annulus area; 2) the wavelength of maximum emission of the radiance (λ_{max}) measured on a 4th-degree fit on the average spectral radiance computed on the annulus.

After converting spectral radiance in irradiance/solar flux (I/F) we compute the two spectral slopes following [5]. These are: 3) 0.4-0.5 μm spectral slope on I/F; 4) 0.5-0.8 μm spectral slope on I/F. The two spectral slopes are computed as angular coefficient ot eh best linear fit in the ranges 0.4-0.5 and 0.5-0.8 μm after having normalized I/F at 0.5 μm. The determination of the spectral indicators follows the scheme shown in Extended Data Figure 1, bottom panels.

Spectral indicators depend from illumination geometries and spacecraft-nucleus distance: as a consequence of the very demanding mission scenario, complex orbits, including terminator, icosahedron, flybys, and far excursions have been flown [31] resulting in a very wide range of distances and solar phases. The correlation between the integrated radiance I and distance is shown in Extended Data Figure 3 where VIRTIS-M measurements are co-located with Rosetta's position and solar phase angle with respect to the comet nucleus along the flight trajectory.

Temporal evolution of the coma colour

The integrated-radiance (I) time-series (Figure 1-a) shows an increase of the coma's brightness starting from January 2015 (MTP012, heliocentric distance 2.55 AU) to perihelion passage (MTP019, 1.24 AU, August 2015). Due to the characteristics of Rosetta's orbit around the nucleus and the different observation strategies implemented during the mission, the completeness of the annulus region on the VIRTIS dataset is reached only on a limited number of observations marked as red points in Figure 1-a. On

the majority of the remaining observations (black points), partial coverage of the annulus is achieved. Notwithstanding the relative scatters of the data introduced by the variability of the observing conditions, some clear trends are identified. A local maximum $25 \leq I \leq 30$ W/(m^2 sr), is measured about one month after perihelion. Two additional intensity peaks are measured at the end of August and September 2015, when a maximum intensity of about 50 W/(m^2 sr) is reached. These peaks are caused by energetic cometary activity - two outbursts observed by VIRTIS on September 13-14 2015 are reported by [37,38] - but appear also to be strongly correlated with the peculiar viewing geometry and spacecraft position with respect to the nucleus: in fact, at the time of these observations, Rosetta was performing far-nucleus excursions, orbiting at greater distances than usual from the nucleus, up to 450 and 1462 km, respectively. As a consequence of the increased distance from the nucleus, VIRTIS-M has recorded higher radiances boosted by the larger column density of dust particles along the line of sight and by the maximum activity occurring immediately after perihelion. After this period the integrated radiance drops rapidly from MTP021 to MTP024 where an average value of 5 W/(m^2 sr) is reached. The maximum integrated radiance measured in MTP020-021 is about a factor 10 more intense than the average value of 5 W/(m^2 sr) measured when the comet was far from the Sun (> 2 AU) on both inbound and outbound legs of the orbit. With the exclusion of the two peaks, a similar asymmetric, or cusp-like trend with a maximum occurring about one month after perihelion, has been measured by other Rosetta's instruments for the water production rate which is associated to the ejection of the dust [3]. Apart from the greater column density, we have clues that larger particle albedo could contribute to the increase of the integrated radiance: according to [4] the albedo of the dust particles increases up to 20% near perihelion for observations acquired at 90° solar phase angle. Similar albedo changes could be the result of a different composition of the dominant grain population in the coma along the orbit, as discussed in the main paper.

The time-series of the wavelength of maximum emission (λ_{max}) (Figure 1-c) shows a cusp-like trend starting from low values dispersed around λ_{max}=0.45 μm on January 2015 (MTP012) on the inbound leg of 67P trajectory to $\lambda_{max} > 0.5$ μm during perihelion passage (MTP019). Moving along the outbound leg of the orbit, the wavelength of maximum emission shifts progressively towards shorter wavelengths, reaching again λ_{max}=0.45 μm in mid-May 2016 (MTP028). While λ_{max} and integrated radiance time-series show a similar time-trend, spectral slopes time-series (Figure 1-b and d) are characterized by a different evolution: at the two extremes of the time-series both 0.4-0.5 μm and 0.5-0.8 μm slopes are almost neutral while at perihelion they reach values dispersed at 5 and 3 μm^{-1}, respectively. The visible colours of the coma show a systematic reddening before perihelion passage and a progressive blueing after it. The concurrent variations occurring on all spectral indicators time-series point to a change in the dust grains composition and grain size distribution with the heliocentric distance.

Temporal evolution of the nucleus colour

When observed at a global scale, 67P surface dust appears very dark (geometric visible albedo 6.2% [39]) and dehydrated, with an average water ice fraction of about 1% dispersed in submicron grains [40,41]. The residual water ice content, if present, on the dust grains ejected from the surface undergoes rapid sublimation once the grain is lifted [20]. The low thermal capacity of the dust (700 J/kg/K) and the high solar flux can raise rapidly the temperature of the grains causing the sublimation of the volatiles. A colour temperature as high as 630 K is measured on dust grains during outbursts [37] and in the

260-320 K range on quiescent coma [4]. Besides, the grains observed by Rosetta's dust instruments appear dehydrated [30,42]. This probably happens because the instruments aboard the spacecraft are not kept at cryogenic temperatures allowing the dispersion of the volatile fraction of the grains after their collection. Beside from dehydration, also grain size distribution plays a role in the changes of the visible colours, as detailed later.

During the pre-perihelion phase, the nucleus' surface shows a progressive blueing until one month after perihelion when the minimum slope is reached in MTP020 (see Figure 2). In this phase, the gas activity removes the dust from the surface with greater efficiency resulting in the exposure of more pristine subsurface material enriched in ices [5,6,22]. This trend is interrupted after the perihelion passage when a progressive surface reddening is observed. Along the outbound trajectory, the gaseous activity progressively settles resulting in the accumulation of dehydrated (red) dust on the surface. This appears to be a general mechanism, occurring on the majority of the nucleus surface, as shown in Figure 2, where the average 0.5-0.8 μm slope is shown for twelve 30 x 30 meters-wide control-areas at one-month time resolution. These control areas, selected between latitude +45.5° and -34.5°, are the ones which have been observed in daylight by VIRTIS during the entire duration of the mission allowing us to follow the seasonal colour cycle developing on the nucleus.

Dust scattering simulations

The simulations are computed following the Bohren-Huffman Mie scattering code [43] to calculate scattering and absorption by a homogenous isotropic sphere. The method relies on the following assumptions: 1) single-scattering approximation, e.g. the solar photons interact with only one particle before reaching the observer. Such a hypothesis is reasonable for the annulus region considered in this work where the optical depth is small; 2) polydisperse spherical grains size distributions with radii of 0.10-0.99 μm (90 bins, 0.01 μm/bins), 1.0-9.9 μm (90 bins, 0.1 μm/bin), 10-50 μm (40 bins, 1 μm/bin); 3) Five different grain compositions are simulated: water ice (optical constants from [44]), organic material [45], troilite [44], amorphous carbon [46] and Mg-silicate [47]. These endmembers are representative of cometary nuclei composition which is made of a macromolecular assemblage in which various organic components (both aromatic and aliphatic), minerals (including silicates, iron-sulfides like pyrrhotite and/or troilite and possibly ammoniated salt) and ices are mixed together [48]; 4) spectral simulations are performed at 27 wavelengths within the 0.35-1.0 μm spectral range; 5) scattering angle θ(=180°-g) is computed at step of 1° from 55° to 155° and then averaged on 4° bins in order to match VIRTIS field-of-view (3.66°).

Following [49] the single scattering intensity is given by:

$$I(\lambda) = S(\lambda)n_{col}(\rho)\sigma q(\lambda)\frac{p(g.\lambda)}{4\pi} \quad \text{(2.)}$$

where S(λ) is the solar flux [50] scaled at the comet's heliocentric distance, n_{col} is the dust column density computed along the line of sight from an observer placed at distance ρ from the nucleus, σ is the grain geometrical cross-section, q(λ) is the scattering efficiency of a single particle and p(g, λ) is the scattering phase function computed at phase g. Rather than modeling the absolute value of the intensity, we limit here our analysis to the changes occurring in the spectral response of the average radiance emitted from the dust. In particular, we focus in the changes of the wavelength of the maximum emission (Figure 1-c) and s2 slope (Figure 1-d) observed at different heliocentric distances. To achieve this

goal we compute the spectral radiance factor, I(λ) expressed in arbitrary units, derived from eq. 2 by removing the factors depending on the dust grain distribution and properties:

$$I(\lambda, g) \propto S(\lambda)q(\lambda)\frac{p(g,\lambda)}{4\pi} \quad (3.)$$

The phase functions show scattering characteristics depending on composition and grain sizes: as a general rule, transparent grains, like water ice, are characterized by a very intense and collimated forward-scattering peak and a complex resonance peaks at intermediate phase angles. Opaque materials, like troilite, show an almost isotropic scattering function. Semi-transparent particles, like ice tholins, have an intermediate behaviour with a prevalence of backscattering response. Grain size plays a fundamental role in the scattering mechanism: in the Rayleigh regime (particle size much smaller than the wavelength) light is equally forward and back-scattered while in geometric regime (particle size much larger than the wavelength) backscattering dominates.
Fixing composition and grain size, the corresponding phase functions at the 27 visible wavelengths allow a derivation of the spectral radiance according to eq. 3.
While p(g, λ) has a smooth response in the Rayleigh and in the geometric scattering regimes, the simulations, in general, show more fluctuations occurring for certain combinations of composition, grain size, and θ angle when the grain sizes are comparable to the wavelength, e.g. at about 1 μm. To mitigate this effect we have computed simulations between 30°≤g≤120°, corresponding to scattering angles 55°≤ θ ≤155° at steps of 1° and then averaged the angular response of p(g, λ) on 4° bins, similar to the VIRTIS field-of-view. Similarly, the p(g) is computed for single grain radius: 0.10-0.99 μm (90 bins, 0.01 μm/bins), 1.0-9.9 μm (90 bins, 0.1 μm/bin), 10-50 μm (40 bins, 1 μm/bin) and then averaged on each of the three families. Following this method, the I(λ,g) (from eq. 3) is derived for each composition and size distribution. The λ_{max} and, after conversion in I/F, the spectral slope s2 are derived on the simulated I(λ,g). The corresponding values are shown in Figures 3 and 4, respectively.

Modeling dust grains composition and size distribution in the coma

To disentangle the viewing and illumination geometry effects from particles' physical properties and to provide a more quantitative assessment of the changes observed in the λ_{max} time-series, the light scattering on grains of different composition and radius has been simulated. Optical and in-situ measurements of the dust grain distribution in 67P coma by Rosetta's instruments have revealed that the particles lie mainly within the 0.1 μm - 1 mm diameter range [51]. For particles smaller than 1 mm the dust size distribution follows a power-law distribution with a coefficient varying between -2 for heliocentric distances beyond 2 AU and -3.7 at perihelion. Conversely, large grains (diameter >1 mm) show a much steeper distribution with a coefficient -4 [52]. Since small grains are the predominant population, in our analysis we preferentially model the spectral behaviour of small (radius < 50 μm) compact grains. A similar grain size range has been also used by [37,38] to model dust optical properties at infrared wavelengths and by [20] to study thermal evolution and depletion of ice in dust aggregates along jets. VIRTIS data are interpreted through the Mie theory which can simulate the scattering properties of spherical grains of radius a and homogeneous composition having x=(2πa/λ)<1000. Such a limit corresponds to a maximum grain radius a=50 μm in the visible spectral range (wavelength 0.35≤λ≤1.0 μm). To simulate the spectral response of larger grains, including fluffy aggregates [7,53], it is

necessary to use geometric optics approximation [54] and it is beyond the scope of this work.

The changes occurring in the spectral radiance scattered by spherical grains of different composition and grain size distribution as a function of the phase angle (g) are computed for homogeneous particles made of possible cometary material endmembers, including water ice, organic ice tholin, troilite, amorphous carbon and Magnesium silicate. For a given composition and phase angle, the single particle phase function $p(g,\lambda)$ modulates the intensity of the scattered spectral radiance.

The theoretical trends of λ_{max} as a function of the scattering angle $\theta=180°$-g for particles of different composition and three grain size distributions (radius=0.10-0.99 μm, 1.0-9.9 μm, 10-50 μm) considered in this work, are shown in Figure 3. In the same figure we display the distribution of λ_{max} as measured from VIRTIS observations (Fig.3-f) selected during six MTP periods encompassing pre-perihelion (MTP015-016), perihelion (MTP020-021) and post-perihelion (MTP027-028) orbital phases. These periods are chosen because they offer the widest spread in scattering angle necessary to discriminate among different compositions and grain size distributions. Our analysis shows that, with the exception of transparent grains, e.g. water ice and organic ice tholin, the response of opaque materials like amorphous carbon (Fig.3-a) and troilite (Fig.3-d) are characterized by a constant λ_{max} at about 0.5 μm for the intermediate (1.0-9.9 μm) and large (10-50 μm) grain sizes distributions across the $60 \le \theta \le 150°$ scattering angle range explored by VIRTIS. These grains are therefore not matching the observed distribution of the λ_{max}. Conversely, opaque-material submicron grains show a significant shift of the λ_{max} towards the red range, especially for $\theta \le 120°$.

Sub micron grains made of Mg-silicate (Fig.3-b) show a linear increase trend of λ_{max} from 0.56 μm at $\theta=60°$ to 0.63 at $\theta=150°$ resulting not compatible with VIRTIS data. On the contrary, the λ_{max} of grains with radii larger than 1 μm is dispersed around 0.55 μm, a value too much red to reproduce VIRTIS data at $\theta>100°$ and too much blue for $\theta<100$.

Water ice grains (Fig.3-e) offer the only solution matching VIRTIS data taken during the pre (MTP015-016) and post-perihelion periods (MTP027-028) at scattering angles $\theta>100°$. During these phases VIRTIS data are dispersed at $\lambda_{max}<0.5$ μm, a behaviour compatible only with the three water ice grain size distributions we have simulated.

Apart water ice, organic material grains (Fig.3-c) are the second endmember showing spectral similarities compatible with 67P particles: the 1-10 μm and 10-50 μm grain sizes responses are in fact characterized by a linear decrease of the λ_{max} from $\theta=60°$ to 120° making them compatible with observations acquired during perihelion and post-perihelion periods. On the contrary, submicron grains show an extreme red colour across the entire range of scattering angles: having a $\lambda_{max} \ge 0.65$ μm they are marginally compatible only with VIRTIS observations taken at low θ angles. If one assumes that during one month, e.g. during the duration of one MTP period, the dominant composition and grain size is preserved, then the VIRTIS measurements taken during MTP028 at $\theta>130°$ could be compatible not only with water ice but also with large (10-50 μm) organic material grains. As shown in Fig.3-a, amorphous carbon sub-micron (0.1-0.9 μm) size grains are characterized by a reddening of the λ_{max} for $\theta<90°$ similar to VIRTIS but with absolute values too low to exactly match the observations. Instead, the match is compatible for $90°<\theta<120°$, making submicron amorphous carbon grains a good interloper between water ice and organic grains. Finally, Mg-silicate (Fig.3-b) and troilite (Fig.3-d) submicron grains show λ_{max} trends at low scattering angles not compatible with VIRTIS data.

Composition and grain size distribution of the dust particles are further analysed through the 0.5-0.8 μm spectral slope (Figure 4) derived form VIRTIS data which shows a peaked distribution at θ=100°-110° (Fig.4-f) occurring on perihelion (MTP020-021) and post perihelion (MTP028) sequences. In our simulations a similar behaviour is compatible with submicron-sized grains made of organic matter (black points in Fig.4-e) or with >1 μm water ice grains (blue and red points in Fig.4-d). The absolute value of the slope on the peak (≈3 $1/\mu m$) measured at perihelion (MTP020, cyan points) is similar to theoretical values for organic matter. Being transparent, water ice particles are characterized by a peculiar behaviour: submicron grains show a blue colour response (negative slope, black points in Fig.4-d) not compatible with any VIRTIS observation while large grains (blue and red points) are neutral to moderately red and could contribute to the VIRTIS observed slope at any θ angle. Opaque grains with sizes >1 μm show an almost constant neutral to moderately red (0.5 $1/\mu m$) slope within the entire scattering angle range (see red and blue points for amorphous carbon in Fig.4-a and troilite in Fig.4-b). We remark that while the λ_{max} trends of Mg-silicate (Fig.3-b) grains are not compatible with VIRTIS data, their spectral slopes values (Fig.4-c) for radius > 1 μm are remarkably similar for measurements taken during the post-perihelion period.

In the Extended Data Table 3 is shown a compatibility scheme of the λ_{max} and 0.5-0.8 μm spectral slope values for the different composition endmembers, grain radius and scattering angle compared to VIRTIS data.

REFERENCES IN METHODS

[31] Vallat, C. et al., The science planning process on the Rosetta mission, Acta Astronautica, 133, 244-257 (2017).

[32] Filacchione, G. et al., On-ground characterization of Rosetta/VIRTIS-M. II. Spatial and radiometric calibrations, Rev. Sci. Instr., 77, 103106-103106-9 (2006).

[33] Acton, C. H., Ancillary data services of NASA's Navigation and Ancillary Information Facility, Planet. Sp. Sci., 44, 65-70 (1996).

[34] Jorda, L., et al., The global shape, density and rotation of Comet 67P/Churyumov-Gerasimenko from preperihelion Rosetta/OSIRIS observations, Icarus, 277, 257-278 (2016).

[35] Filacchione, G., Calibrazioni a terra e prestazioni in volo di spettrometri ad immagine nel visibile e nel vicino infrarosso per l'esplorazione planetaria, Ph.D thesis, Università di Napoli Federico II, 316 pages (2006).

[36] Bohlin, R. C. and Gilliland, R. L., Hubble Space Telescope Absolute Spectrophotometry of Vega from the Far-Ultraviolet to the Infrared, Astron. J., 127, 3508-3515 (2004).

[37] Bockelée-Morvan, D. et al., Comet 67P outbursts and quiescent coma at 1.3 AU from the Sun: dust properties from Rosetta/VIRTIS-H observations, Mon. Not. R. Astron. Soc., 469, S443-S458 (2017).

[38] Rinaldi, G. et al., Summer outbursts in the coma of comet 67P/Churyumov–Gerasimenko as observed by Rosetta–VIRTIS, Mon. Not. R. Astron. Soc., 481, 1235-1250 (2018).

[39] Ciarniello, M. et al., Photometric properties of comet 67P/Churyumov-Gerasimenko from VIRTIS-M onboard Rosetta, Astron. Astrophys., 583, A31 (2015).

[40] Capaccioni, F., et al., The organic-rich surface of comet 67P/Churyumov-Gerasimenko as seen by VIRTIS/Rosetta, Science 347, 6220, aaa0628 (2015).

[41] Raponi, A., et al., The temporal evolution of exposed water ice-rich areas on the surface of 67P/Churyumov-Gerasimenko: spectral analysis, Mon. Not. R. Astron. Soc., 462, 476-490 (2016).

[42] Hilchenbach, M. et al. Comet 67P/Churyumov-Gerasimenko: Close-up on Dust Particle Fragments, Astrophys. J. L., 816, L32, 6pp (2016).

[43] Bohren, C. F. and Huffman, D. R., Absorption and scattering of light by small particles, Wiley, New York (1983).

[44] Pollack, J. B., et al., Composition and radiative properties of grains in molecular clouds and accretion disks, Astrophys. J. S., 421, 615-639 (1994).

[45] Cuzzi, J. N., Estrada, P. R., Sanford, D. S., Utilitarian Opacity Model for Aggregate Particles in Protoplanetary Nebulae and Exoplanet Atmospheres, Astrophys. J. S., 210, id21, 18 pp (2014).

[46] Zubko, V.G. et al., Optical constants of cosmic carbon analogue grains - I. Simulation of clustering by a modified continuous distribution of ellipsoids, Mon. Not. R. Astron. Soc., 282, 1321-1329 (1996).

[47] Dorschner et al., Steps towards interstellar silicate mineralogy II. Study of Mg-Fe-silicate glasses of variable composition, Astron. Astrophys., 300, 503–520 (1995).

[48] Filacchione, G. et al., Comet 67P/CG Nucleus Composition and Comparison to Other Comets, Space Sci. Rev., 215:19 (2019)

[49] Fink, U & Rinaldi, G., Coma dust scattering concepts applied to the Rosetta mission, Icarus, 257, 9-22 (2015).

[50] Kurucz R. L, in Rabin D. M., Jefferies J. T., Lindsey C. eds, Proc. IAU Symp. 154, Infrared Solar Physics, Kluwer, Dordrecht, p. 523 (1994).

[51] Rotundi, A., Dust measurements in the coma of comet 67P/Churyumov-Gerasimenko inbound to the Sun, Science 347, 6220, aaa3905 (2015).

[52] Fulle, M. et al., Evolution of the Dust Size Distribution of Comet 67P/Churyumov-Gerasimenko from 2.2 au to Perihelion, Astrophys. J., 821, 19 (2016).

[53] Fulle, M. et al., Density and Charge of Pristine Fluffy Particles from Comet 67P/Churyumov-Gerasimenko, Astrophys. J. L., 802, L12, 5 pp (2015).

[54] Grynko Y., Shkuratov Y.G., Light scattering from particulate surfaces in geometrical optics approximation. In: Kokhanovsky A.A. (eds) Light Scattering Reviews 3. Springer Praxis, doi.org/10.1007/978-3-540-48546-9_9 (2008).

EXTENDED DATA

| Period	Start Time	End Time	Heliocentric distance (AU)
MTP012	2015-01-13T23:28:53	2015-02-10T23:23:53	2.552-2.344
MTP013	2015-02-10T23:23:53	2015-03-10T23:23:53	2.344-2.130
MTP014	2015-03-10T23:23:53	2015-04-08T23:23:53	2.130-1.967
MTP015	2015-04-08T23:23:53	2015-05-05T23:23:53	1.967-1.703
MTP016	2015-05-05T23:23:53	2015-06-02T23:23:53	1.703-1.508
MTP017	2015-06-02T23:23:53	2015-06-30T23:23:53	1.508-1.350
MTP018	2015-06-30T23:23:53	2015-07-28T23:23:52	1.350-1.257
MTP019	2015-07-28T23:23:52	2015-08-25T23:23:52	1.257-1.253
MTP020	2015-08-25T23:23:52	2015-09-22T23:23:52	1.253-1.340
MTP021	2015-09-22T23:23:52	2015-10-20T23:23:52	1.340-1.494
MTP022	2015-10-20T23:23:52	2015-11-17T23:23:52	1.494-1.686
MTP023	2015-11-17T23:23:52	2015-12-15T23:28:52	1.686-1.897
MTP024	2015-12-15T23:28:52	2016-01-12T23:28:52	1.897-2.113
MTP025	2016-01-12T23:28:52	2016-02-09T23:28:52	2.113-2.327
MTP026	2016-02-09T23:28:52	2016-03-08T23:28:52	2.327-2.536
MTP027	2016-03-08T23:28:52	2016-04-05T23:28:52	2.536-2.738
MTP028	2016-04-05T23:28:52	2016-05-03T23:27:51	2.738-2.933

Extended Data Table 1. Rosetta's calendar MTP (Medium Term Plan) periods dates and heliocentric distance.
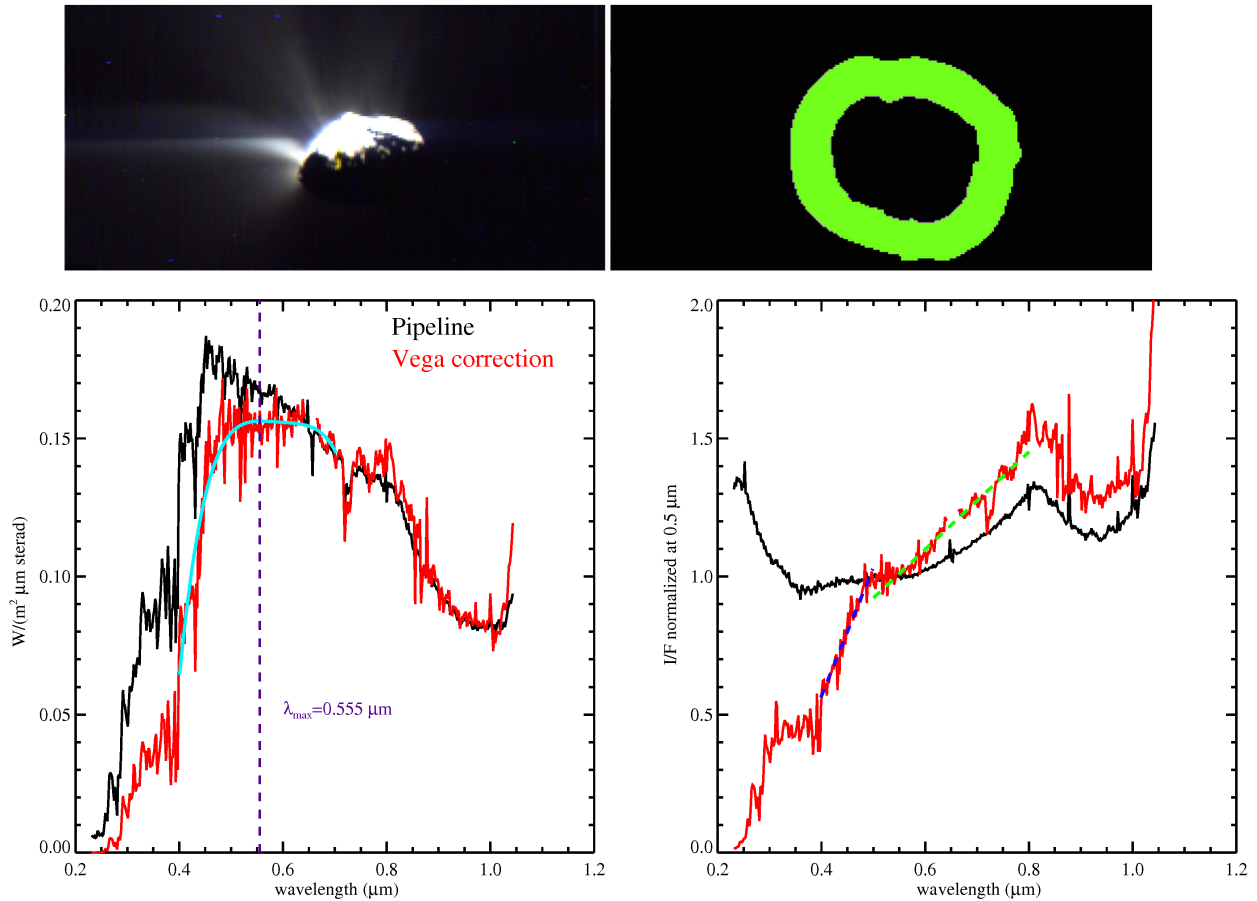
Extended Data Figure 1. Example of a typical VIRTIS-M observation of 67P nucleus and coma. Top Left Panel: visible colours RGB=(0.7, 0.55, 0.44 μm) image, stretched to saturate the nucleus and enhance jets visibility in the coma. Top Right Panel: tangent altitude image where the green mask corresponds to the annulus containing all pixels having a tangent altitude between 1 and 2.5 km from the limb. Bottom Left Panel: Average Radiance spectra as derived from official pipeline (black curve) and after correction with Vega data (red curve). The 4th degree polynomial fit to the corrected radiance is shown (cyan curve). The retrieved maximum emission wavelength on the fit is indicated by the magenta dashed line. Bottom Right Panel: corresponding I/F spectra normalized at 0.5 μm. The best-fitting slopes in the 0.4-0.5 and 0.5-0.8 μm ranges are indicated by blue and green dashed lines, respectively.

Observation	Start Time	End Time	(Band, Sample, Line)	Int. Time (s)
V1_00402035638.QUB	2015-09-28T04:35:17.781	05:04:11.405	(432,256,29)	50
V1_00403369562.QUB	2015-10-13T15:07:22.178	15:38:15.817	(432,256,31)	50
V1_00403848118.QUB	2015-10-19T04:03:18.373	04:34:12.013	(432,256,31)	50
V1_00406049718.QUB	2015-11-13T15:36:39.065	16:03:32.757	(432,256,27)	50

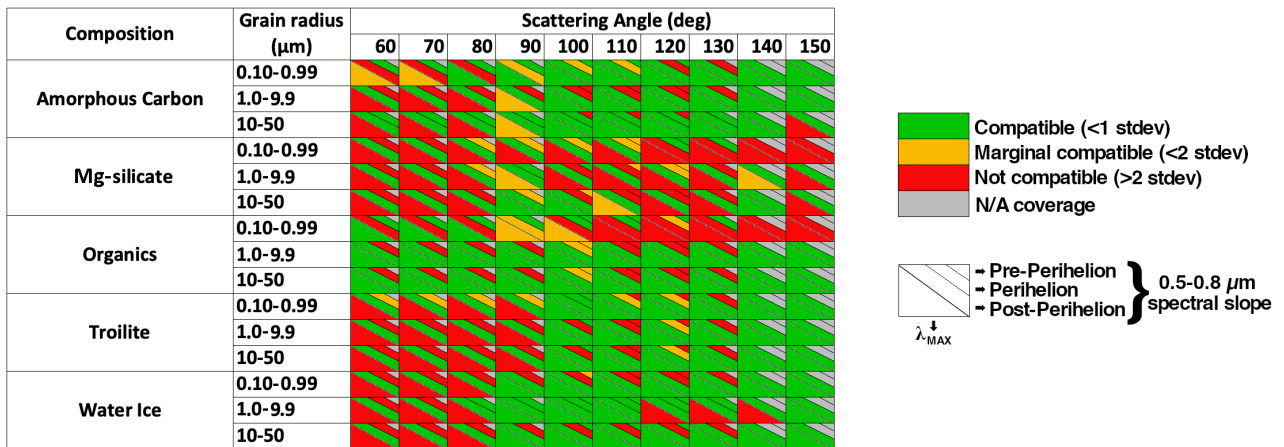Extended Data Table 2. Vega observations listing.
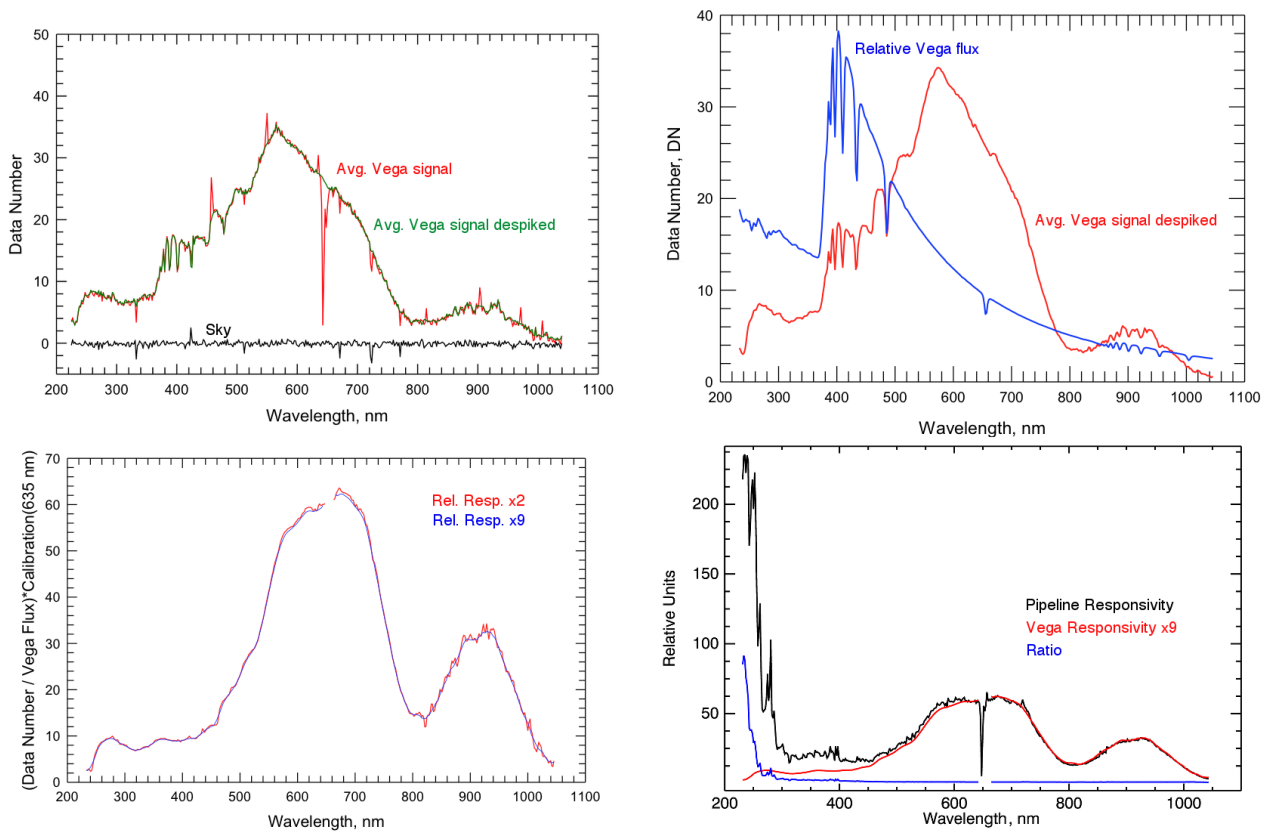
Extended Data Figure 2. Vega star signal and derived VIRTIS responsivity. Top left: average spectrum of Vega, in DN, from observation V1_00402035638.QUB (red curve) and spectrum corrected for dark current, despiked, and filter notch removed (green curve). Note the correlation of negative spikes in the Vega and average sky spectrum (black curve). Due to the instrumental point spread function and spectral tilt, the signal is an average taken from 18 pixels. Top right: average spectrum of Vega derived from the four observations listed in Extended Data Table 2 after having applied a processing similar to the one shown in the previous plot. The curve is averaged with a 2-point running boxcar filter. The Vega flux [36] is shown in relative units (blue curve); Bottom left: VIRTIS responsivity derived from Vega signal averaged with a 2-point running boxcar filter (red curve) and 9 points (blue curve) after normalization at 0.635 μm above the standard responsivity value. Bottom right: comparison between standard pipeline (black curve) and Vega responsivities with a 9-point running boxcar filter(red curve). The ratio between the two responses is the blue curve.
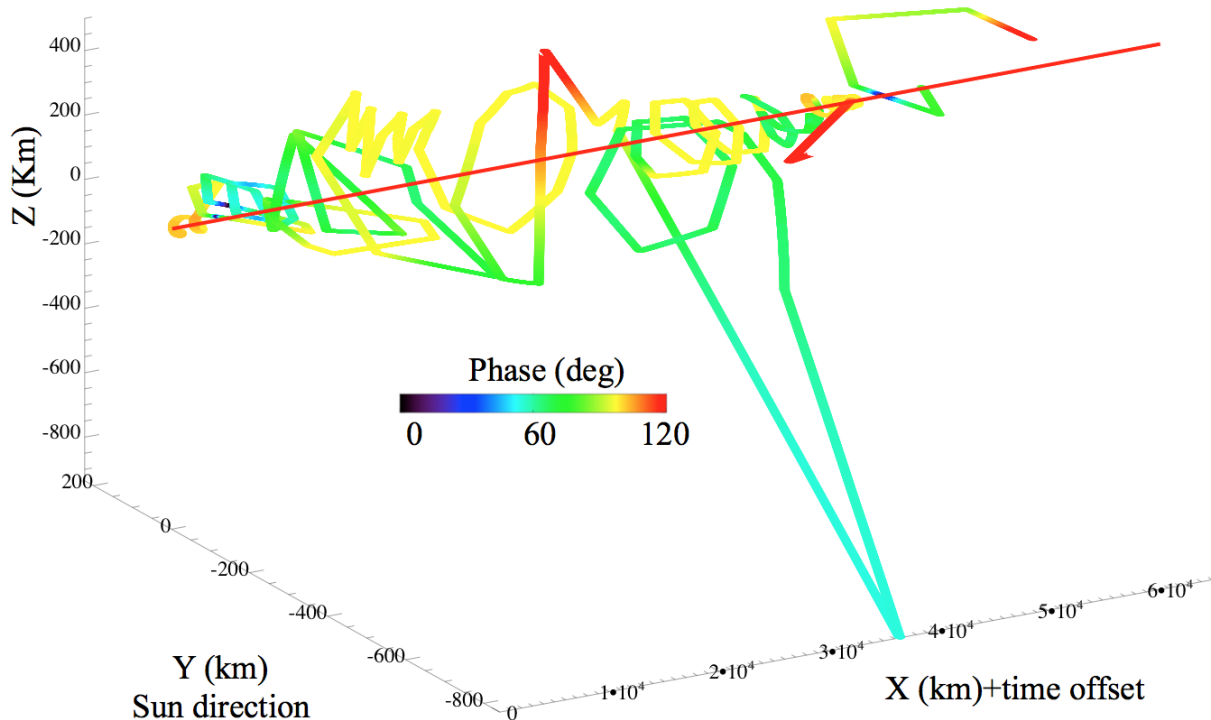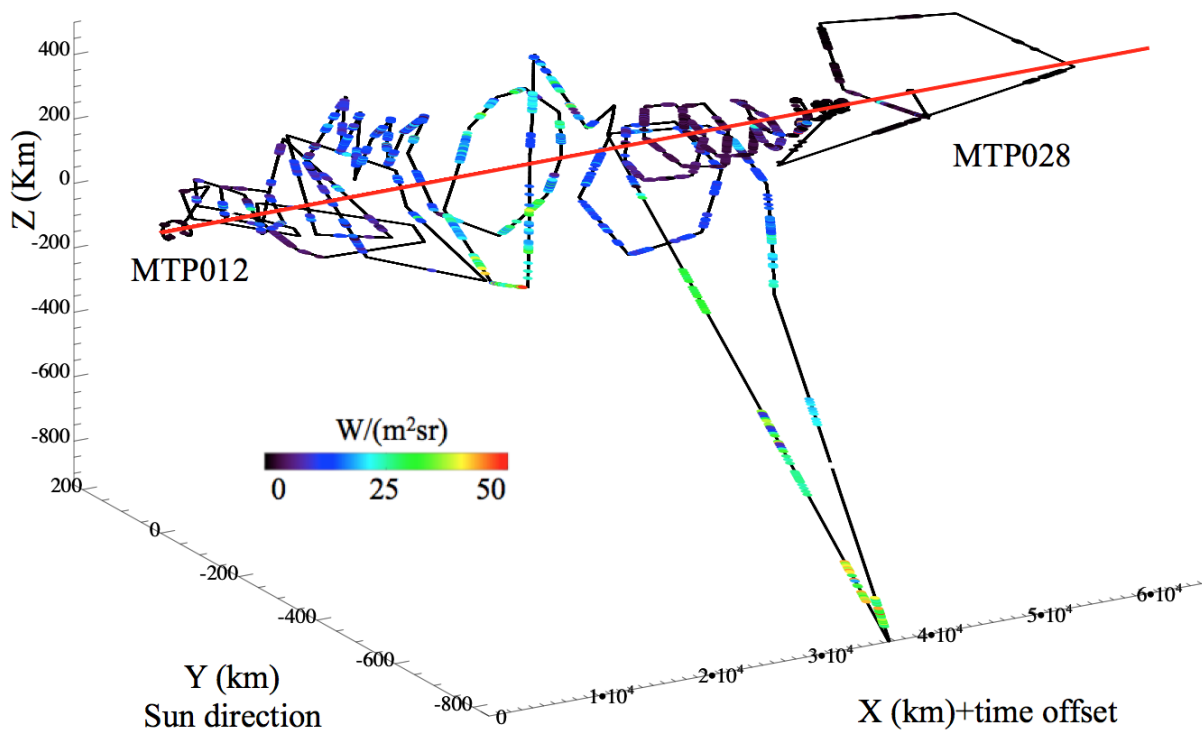
Extended Data Figure 3. Rosetta spacecraft 3d trajectory and solar phase angle variations during the time. Top panel: Rosetta trajectory in the 67P XYZ reference frame. Points along the X axis are shown starting from Rosetta's position at 2015-01-13T23:28:53 (MTP012) with an increment of 1 km every 20 minutes to improve visualization. Y axis is oriented towards the Sun and Z perpendicular to the orbital plane. The red line indicates the position of the nucleus along the X axis. The integrated radiance as measured on each

observation is reported according to the colour scale. Bottom Panel: variation of the solar phase angle (Sun-nucleus centre-Rosetta) during the mission.

Extended Data Table 3. Summary scheme showing spectral indicators (λ_{MAX}, 0.5-0.8 μm spectral slopes) compatibility between VIRTIS observations and Mie scattering simulations for a given composition, grain radius range and scattering angle.